

Discovery of a radio lobe in the Cloverleaf Quasar at $z = 2.56$

Lei Zhang,^{1,2} Zhi-Yu Zhang,^{1,2} ^{*} James. W. Nightingale,³ Ze-Cheng Zou,¹ Xiaoyue Cao,^{4,5,6}
 Chao-Wei Tsai,⁵ Chentao Yang,^{7,8} Yong Shi,^{1,2} Junzhi Wang,^{9,10} Dandan Xu,¹¹ Ling-Rui Lin,^{1,2}
 Jing Zhou,^{1,2} Ran Li,^{6,5,4}

¹ School of Astronomy and Space Science, Nanjing University, Nanjing 210023, People's Republic of China

² Key Laboratory of Modern Astronomy and Astrophysics (Nanjing University), Ministry of Education, Nanjing 210023, People's Republic of China

³ Department of Physics, Institute for Computational Cosmology, Durham University, South Road, Durham DH1 3LE, UK

⁴ School of Astronomy and Space Science, University of Chinese Academy of Sciences, Beijing 100049, People's Republic of China

⁵ National Astronomical Observatories, Chinese Academy of Sciences, 20A Datun Road, Chaoyang District, Beijing 100012, People's Republic of China

⁶ Institute for Frontiers in Astronomy and Astrophysics, Beijing Normal University, Beijing 102206, People's Republic of China

⁷ Department of Space, Earth and Environment, Chalmers University of Technology, Onsala Space Observatory, SE-439 92 Onsala, Sweden

⁸ European Southern Observatory, Alonso de Córdova 3107, Vitacura, Casilla 19001, Santiago de Chile, Chile

⁹ Shanghai Astronomical Observatory, Chinese Academy of Science, 80 Nandan Road, Shanghai 200030, People's Republic of China

¹⁰ Department of Physics, Guangxi University, Nanning 530004, People's Republic of China

¹¹ Department of Astronomy, Tsinghua University, Beijing 100084, China

Accepted XXX. Received YYY; in original form ZZZ

ABSTRACT

The fast growth of supermassive black holes and their feedback to the host galaxies play an important role in regulating the evolution of galaxies, especially in the early Universe. However, due to cosmological dimming and the limited angular resolution of most observations, it is difficult to resolve the feedback from the active galactic nuclei (AGN) to their host galaxies. Gravitational lensing, for its magnification, provides a powerful tool to spatially differentiate emission originated from AGN and host galaxy at high redshifts. Here we report a discovery of a radio lobe in a strongly lensed starburst quasar, H1413+117 or Cloverleaf at redshift $z = 2.56$, based on observational data at optical, sub-millimetre, and radio wavelengths. With both parametric and non-parametric lens models and with reconstructed images on the source plane, we find a differentially lensed, kpc scaled, single-sided radio lobe, located at ~ 1.2 kpc to the north west of the host galaxy on the source plane. From the spectral energy distribution in radio bands, we find that the radio lobe has an energy turning point residing between 1.5 GHz and 8 GHz, indicating an age of 20–50 Myr. This could indicate a feedback switching of Cloverleaf quasar from the jet mode to the quasar mode.

Key words: gravitational lensing; strong – galaxies: high-redshift – submillimetre: galaxies.

1 INTRODUCTION

The correlated growth of the bulge mass of a galaxy and its supermassive black hole (SMBH) mass throughout cosmic time has been described as their co-evolution (Ferrarese & Ford 2005; Kormendy & Ho 2013). When the SMBH actively accretes, Active galactic nucleus (AGN) turns on, which can drive powerful feedback to the surrounding interstellar medium (ISM) of the host galaxy. The radiation pressure and the energetic particles in the AGN wind and jet behave as the main forms of the feedback. The feedback process can sweep and heat up the cold gas along its radial paths, and as a result, quench the star formation (Springel et al. 2005; McNamara & Nulsen 2007; Cattaneo et al. 2009). For the high-luminosity quasars, the host galaxy and surrounding environment receive powerful feedback from its AGN through electromagnetic radiation (known as quasar mode), kinetic jets (known as radio mode), or both (Fabian 2012; Kormendy & Ho 2013; Churazov et al. 2005).

Similar to the cosmic star formation, the evolution of quasi-stellar object (QSO) activity also shows a strong cosmic evolution, reaching its peak at $z \sim 2$ (e.g., Schmidt & Green 1983; Wolf et al. 2003). The feedback of QSOs in this era is therefore considered as the key mechanism to quench star formation. Galactic outflows driven by AGNs (e.g., Farrah et al. 2012; Cano-Díaz et al. 2012; Nesvadba et al. 2011; Alexander et al. 2010; Prochaska & Hennawi 2009; Nesvadba et al. 2008) have shown evidence of quenching. High-velocity galactic winds, which are commonly detected with the broad absorption lines against a strong quasar continuum (e.g., Dunn et al. 2010; Moe et al. 2009; Saez et al. 2009) and also evidenced with highly-ionized Fe lines in low-luminosity AGNs (Shi et al. 2021), can efficiently remove the ISM from the host galaxies. On the other hand, radio lobes/jets (e.g., Gopal-Krishna & Wiita 2001; McNamara & Nulsen 2007; Cattaneo & Best 2009; Cattaneo et al. 2009; Fabian 2012), which are often discovered on scales from several tens of kpc to Mpc, can also directly impact star formation.

However, the majority of high-redshift QSOs have very compact sizes (Silverman et al. 2019; Li et al. 2021; Ding et al. 2022), which

* E-mail: zzhang@nju.edu.cn

limits the separation between their host galaxy and AGN-related components. Multiple-wavelength observations with spatial resolutions on scales of sub-kpc are therefore needed, which are still extremely difficult, given the capability of current instruments and cosmological dimming effects (Lanzetta et al. 2002).

Gravitational lensing serves as a powerful tool to improve both sensitivity and spatial resolution. With proper demagnification modelling, the lensing system allows us to resolve the detailed galactic structures of high- z QSOs for case studies. Cloverleaf (also known as H1413+117) is one such target. Discovered by Magain et al. (1988), it is a strongly lensed starburst galaxy with a bright AGN at $z = 2.558$. It contains four images at both optical and sub-millimetre wavelengths (Kneib et al. 1998). With the detections of CO, HCN, and FIR emission, Cloverleaf is confirmed to contain an extensive molecular disc of ~ 1.6 kpc in diameter, a molecular gas mass of $2 \times 10^{10} M_{\odot}$, and a star formation rate of $10^3 M_{\odot} \text{ yr}^{-1}$ (Solomon et al. 2003; Venturini & Solomon 2003; Barvainis et al. 1997; Weiß et al. 2003). On the other hand, information about this system in the lens plane is limited due to the lens galaxy’s faint emission (Lawrence 1996; Angonin et al. 1990; Turnshek et al. 1997), while Chantry & Magain (2007) suggested a deconvolved lens image from Hubble Space Telescope (HST) *F160W* and *F160W* data. The redshift of the lens galaxy is derived from the H α narrow absorption systems (Turnshek et al. 1988; Magain et al. 1988) at $z \sim 1.7$.

With the latest high-sensitivity, high-resolution, and high-fidelity data of Cloverleaf system from ALMA, VLA, and HST, we are able to not only compare morphologies from different gas phases but also constrain the lens galaxy mass models more accurately than previous models. The traditional method (Kneib et al. 1998), which is based on parametric modelling, has limitations in the cases of irregular sources. The newly developed non-parametric modelling, which is required for high angular resolution and high sensitivity analysis, greatly improves the reconstructed source plane (Nightingale & Dye 2015; Nightingale et al. 2018) and thus the structures of Cloverleaf system can be well distinguished.

This work focuses on observational data at three wavelengths: (i) optical, which is dominated by the QSO emission and is seen as almost four point sources from HST images (Kneib et al. 1998); (ii) Sub-millimetre, which traces the gaseous dusty disk of the host galaxy (Solomon et al. 2003; Granato et al. 1996), with current ALMA observations having enough resolution to resolve the four images and; (iii) radio, where the low frequency (e.g., 1–10 GHz) radio emission traces relativistic charged particles accelerated by the radio jet (Kayser et al. 1990) launched by the central AGN or starburst. The high-frequency (e.g., 10–30 GHz) radio continuum may also have contributions from the free-free emission and/or the dust emission originated in the host galaxy. With these data, we can separate the AGN contribution from the host galaxy.

This paper is organized as follows: Observations and data reduction are presented in Section 2. The modelling processes, the lens models of the host galaxy, and the newly discovered radio lobe, which are built up with both parametric and non-parametric models, are shown in Section 3. In Section 4, we analyse the spatial distribution, the spectral energy distribution of radio emission, and the differential lensing effect. In Section 5, we discuss the confirmation, emission components, and the age of this radio lobe. Last, we conclude the summary in Section 6.

Throughout the paper, we assume a cosmology with $\Omega_m = 0.310$, $\Omega_{\Lambda} = 0.689$, and $H_0 = 67.7 \text{ km s}^{-1} \text{ Mpc}^{-1}$ (Planck Collaboration et al. 2020). In this case, $1''$ corresponds to ~ 8.7 kpc in the lens plane at $z = 1.7$ and ~ 8.22 kpc in the source plane at $z = 2.56$.

2 MULTI-BAND OBSERVATIONAL DATA AND DATA REDUCTION

We obtain multi-wavelength, high-angular-resolution data from the archival systems of HST (optical), ALMA (sub-millimetre), VLA (radio), and e-Merlin (radio).

2.1 HST F814W Image

The optical image is obtained from the HST archive. This three-orbit observation was performed on 26th Jan 2000, with the Advanced Camera for Surveys (ACS) and the F814W filter. We choose the ACS images for their high spatial sampling rate of $0.05'' \text{ pix}^{-1}$ (Lucas & Rose 2021). We stacked all ACS images with SWARP (Bertin et al. 2002). We use `IMFIT` in Common Astronomy Software Applications version 6.1.2.7 (CASA) (McMullin et al. 2007) to fit a star located at (14 : 15 : 47.39856, +11 : 29 : 50.7480) (2MASS id: J14154739+1129507 (Cutri et al. 2003)) in the field and obtain its full width at half maximum (FWHM) to be ~ 0.08 arcsec, which is adopted as the image resolution. The rms noise is evaluated to $0.2 \text{ erg s}^{-1} \text{ cm}^{-2} \text{ \AA}^{-1}$ (below referred as counts).

2.2 ALMA 300 GHz continuum

We adopt the ALMA archival data from projects 2012.1.00175.S (PI: van der Werf, Paul) and 2017.1.00963.S (PI: Sharon, Chelsea), both observed at Band 7 (see Table 1 for observational details).

We calibrate the raw data with CASA (version 6.1.2.7 McMullin et al. 2007) with the associated standard pipeline. Then we combine all the calibrated on-source data and omit the frequency range of CO $J=11-10$. We invert the combined visibility data by task `TCLEAN` with the ‘`dfs`’ mode, a gridding of `MOSAIC`, a cell size of $0.02''$, and a Briggs weighting with a `ROBUST` of 1.5. The synthesised image (see Fig. 1 right) has a beam size of $0.26'' \times 0.20''$ and a position angle of -31 deg. The noise level is $35 \mu\text{Jy beam}^{-1}$, estimated from the emission-free area in the field.

2.3 VLA Archival data

2.3.1 VLA 8 GHz continuum

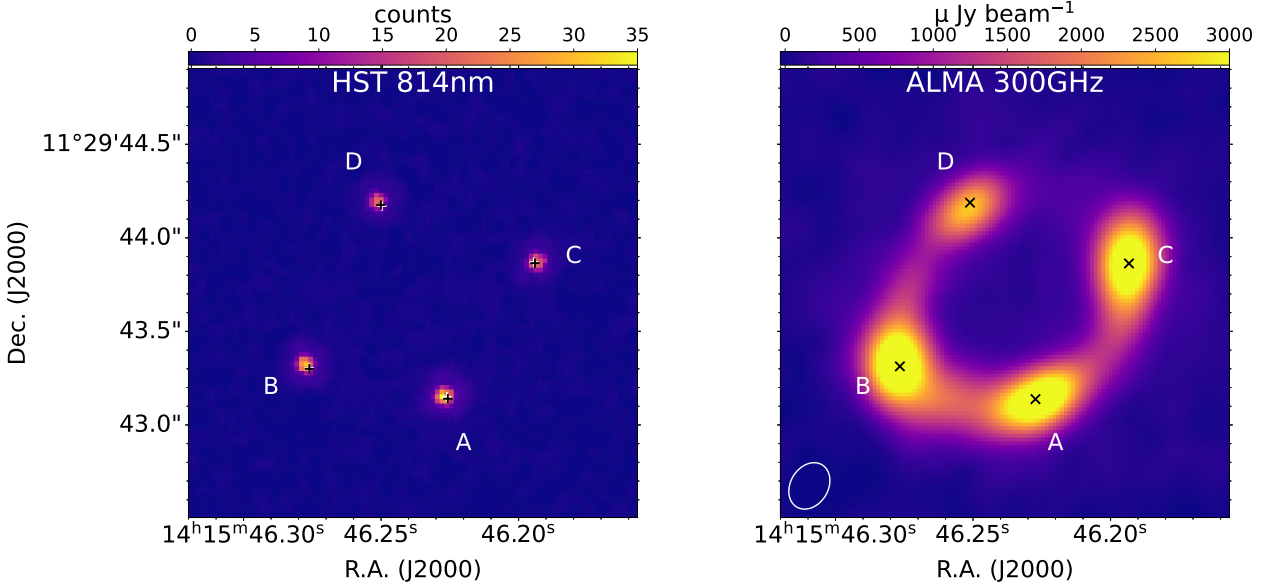
The Very Large Array (VLA) 8 GHz data were obtained from the NRAO archive¹. The project IDs are AS357 and AC243, which were performed on 13 Jan. 1989 and 04 Feb. 1989, respectively. Both observations were done with the A-configuration of the VLA. The total observing time was ~ 5 hours and 4 hours, with ~ 1.5 hours and 1 hour effective on-source time, respectively. Each on-source scan took 15 minutes and 10 minutes with a sampling time of 1 second. In both observations, 3C 286 (1328+307) was adopted as both flux and bandpass calibrators, while the phase calibrator was 1413+135. The receivers were configured with two spectral line windows (SPW), centring at 8.415 and 8.464 GHz, respectively. Each SPW covers a 50 MHz bandwidth, offering a total bandwidth of 100 MHz, with full stock polarisations. The baselines of both observations range from 15 k λ to 950 k λ in the UV space.

The data was first imported to AIPS and converted to the `UVFITS` format. We use `CASA` (ver. 6.1.0) to calibrate the data manually following standard procedures. We then image the data with task `TCLEAN` in `CASA`, with the ‘`dfs`’ mode. We adopted natural weighting to ensure

¹ <https://data.nrao.edu/portal>

Table 1. Details of the observations on Cloverleaf from the ALMA data archive.

Proj. ID	Date	Calibrators		Freq. Coverage		Baseline $k\lambda$	Time min
		Gain	Flux/BP	LSB (GHz)	USB (GHz)		
2012.1.00175.S	25 Jun. 2015	Titan	J1415+1320	325.86–329.28	338.43–341.46	28–1433	68
2012.1.00175.S	30 Jun. 2015	J1550+054	J1415+1320	276.68–279.62	289.50–292.43	36–1530	9
2012.1.00175.S	27 Sep. 2015	J1550+054	J1415+1320	311.93–314.43	325.86–327.85	40–2414	17
2017.1.00963.S	22 May. 2018	J1337+1257	J1347+1217	341.42–345.04	353.42–357.04	14–372	5

**Figure 1.** Cloverleaf at optical and sub-millimetre bands: Left: HST optical data where components A, B, C and D are four images of this lensing system; the black pluses and the white pluses mark the peak positions of the model images with the parametric and the non-parametric model respectively. Right: dust continuum data around 300 GHz where the black crosses mark the peak positions of four components in the HST data.

maximised sensitivity. The final synthesised beam is $0.32'' \times 0.27''$ with a position angle of -33 deg. We then convert the equatorial coordinate from the B1950 epoch to the J2000 epoch with task `IMREGRID`. The rms noise level is $\sim 5.0 \mu\text{Jy beam}^{-1}$.

2.3.2 VLA 33 GHz continuum

We obtained the K-a band JVLA data from the NRAO archival system. The project number is 13B-051 (PI: Sharon, Chelsea). This project consists of a total of 18 execution blocks (EBs) targeting Cloverleaf. However, three of them, taken before 22 Oct. 2013, were corrupted and not usable due to incomplete execution. The remaining 15 EBs were taken from 27 Oct. 2013 to 5 Jan. 2014, with the B-array configuration. The pointing observations were performed at the X-band, and the observations were performed at the K-a band. These observations adopted 27 antennas and took a total of ~ 6.8 hours on source.

The receiver covers a frequency range of 31.95–34.00 GHz, with 16 spectral line windows (128 MHz each) and two polarisations. The total bandwidth is ~ 2 GHz. The bandpass/flux calibrator and the gain calibrator are 3C 286 and J1415+1320, respectively. The baselines range from $16 k\lambda$ to $1192 k\lambda$.

We calibrate the raw data using CASA (ver. 5.6.2-2) with the standard VLA data reduction pipeline. Then we combine all calibrated data and abandon the spectral windows that contain the CO $J=1 \rightarrow 0$ line emission. To save computational resources, we bin all channels

for each spectral line window. Considering a maximum offset of $\sim 2''$ from the phase centre, the bandwidth smearing effect is negligible ($(\Delta\nu/\nu_0) \times (\theta_{\text{offset}}/\theta_{\text{HPBW}}) \leq 0.026$) for Cloverleaf. Then we image the visibility data with CASA (ver. 6.1.2.7), using task `TCLEAN`. We adopted the ‘mfs’ mode, a gridding of `STANDARD`, a cell size of $0.05''$, and a Briggs weighting with a `ROBUST` of 1.5. The cleaned image has a restoring beam size of $0.26'' \times 0.23''$ with a position angle of -37 deg. The rms noise level is $\sim 4.6 \mu\text{Jy beam}^{-1}$.

2.4 E-Merlin 1.5 GHz continuum data

The e-Merlin 1.5 GHz data was obtained from the e-Merlin archival system. The project number is CY4215. The observation was performed on 09 Feb. 2017, with a total observing time of 13 hours. The receiver covers a frequency range of 1.25–1.77 GHz, with eight spectral windows, of which each has 64 MHz sampled with 128 channels. The total bandwidth is 512 MHz. The average sampling time is 2.0 seconds.

In total, seven antennas were adopted during the observations. The bandpass and flux calibrator was 1331+305 (3C286), and the gain calibrator was 1415+1320. Every 10 minutes the telescope switch between the target (7 minutes) and the gain calibrator (3 minutes). The observations spanned ~ 7.7 hours on source in total. The baselines range from $24 k\lambda$ to $1276 k\lambda$ in the UV space.

The archival data has been correlated but not calibrated. We first convert the common uvfits format to the format of ‘measurement

set’ and use *CASA* (ver. 6.1.0) to flag the data and calibrate manually. For imaging, we adopted the ‘mfs’ mode, a gridding of *STANDARD*, a cell size of 0.05 arcsec, and a Briggs weighting scheme with a *ROBUST* of 1.5. The cleaned image has a default restoring beam size of $0.26'' \times 0.18''$ with a position angle of 25 deg. The rms noise level is $\sim 47 \mu\text{Jy beam}^{-1}$.

In the spectral slope index analysis, we use a restoring beam of $0.25''$ when restoring the radio images, to analyse these data with the same reconstructed source plane. We also clean the e-Merlin data with a *nterm* of 2 to get the local spectral index map on the image plane (see Fig. 5).

2.5 Astrometric correction

We notice a systematic astrometric position offset between the HST image and those at radio/submm bands, which is unlikely caused by the differential lensing effect. We fit the peak positions of the four images with SAOimageDS9 (Joye & Mandel 2003) for both the HST data and the ALMA continuum data. From these, we get an average offset of $0.126''$ in the right ascension (R.A.) and $0.219''$ in the declination (Dec.). After we corrected the offset, the peak positions of the images obtained from HST and ALMA (see Fig. 1) are still not yet perfectly aligned (though the current offsets are within one pixel of the HST image), which may originate from different emission areas and/or imperfections of the observations.

3 LENS MODELLING

To analyse the detailed morphology of multi-wavelength images in the source plane, we adopt the lens model software *PyAutoLens* (*AutoLens*)² (Nightingale et al. 2021b; Nightingale & Dye 2015; Nightingale et al. 2018). We model Cloverleaf with both parametric and non-parametric models for the lensed source galaxy, following the visual step-by-step guide provided in *PyAutoLens*³.

We take the assumption from Kneib et al. (1998) that the lens system is contributed by a single galaxy (the narrow absorption systems) and a distant cluster both at $z \sim 1.7$.

3.1 Overview of Lens Modelling Strategy

We perform lens modelling with the following series of linked heuristic steps:

- Fit the HST data using a simple lens model which assumes point-source emission for the source galaxy. This provides an initial estimate for the parametric lens mass model.
- Take the highest likelihood results from the previous step as the initial input to fit the ALMA 300 GHz continuum data with another parametric mass model, using an extended source model which follows a smoothly parameterized form of elliptical Sérsic profile.
- Using the mass model inferred in the previous step to initialise the fit, fit different waveband datasets with a non-parametric source reconstruction which uses a Voronoi mesh.

In our lens model, the redshift of the lens plane is set as 1.7 (Kneib et al. 1998).

² <https://github.com/Jammy2211/PyAutoLens>

³ Both parametric and non-parametric fitting methods are provided as Jupyter notebooks at the following link: https://github.com/Jammy2211/autolens_likelihood_function

3.2 Parametric fitting—optical and sub-mm images

3.2.1 The HST optical data

The HST optical (814 nm) image is shown in the left panel of Fig. 1. We use *IMFIT* to measure the sizes (FWHM) of the four components (see Table 2), by assuming that they follow Gaussian distributions. The fitted FWHMs of all four components are almost identical to the FWHM of a point source ($\sim 0.08''$), so all these images can be treated as compact point sources without extended structures, which is also consistent with the result that the optical emission is dominated by a point-like AGN in the literature (Magain et al. 1988).

First, to model the HST data, we adopt an isothermal ellipsoid with an external shear for the lens galaxy’s mass and use a “point” to represent the source galaxy. With this optical-band lens modelling, we can preliminary estimate the lens mass model, as well as the source’s flux and position.

The four optical images of Cloverleaf point sources may suffer from micro-lensing (Kayser et al. 1990), which may lead to a biased result since the micro-lensing effect is not included in the strong lens modelling. Additionally, the limited number of data (i.e., flux and position) provided by the four lensed images only barely constrain the lens model, resulting in considerable uncertainties. These two limitations beg for a refined analysis at the submillimeter band, on which we perform the lens modelling with an extended lensed arc and use the modelling result of the optical band as a prior. The extended lensed arc at the submillimeter wavelength is not subject to the micro-lensing effect, and its entire brightness distribution can be used to improve the precision of the lens model.

3.2.2 The ALMA 300 GHz continuum

We next fit the ALMA 300 GHz sub-millimetre data with a more complex parametric lens model. We adopt a power-law ellipsoid (Tessore & Metcalf 2015) with an external shear as the lens galaxy mass profile, and model the source with an elliptical Sérsic profile.

We fix the centre of the lens mass model (from the result of the HST data modelling) to reduce the dimensions of parametric space. All remaining parameters from the previous model are then used to create the initial input for this modelling. The inferred parameters of the best fitting model at $1 - \sigma$ confidence are shown in Table 3, including the centre positions (x & y), the elliptical components (e_x & e_y), the Einstein radius (r), the slope of the power-law profile (α), and the elliptical components of the external shear (e_x & e_y).

3.3 Non-parametric fitting

Non-parametric source reconstructions with *PyAutoLens* are performed using a Voronoi mesh, where the Voronoi cells adapt to the source morphology. In this way, relatively higher resolution is dedicated to its bright central regions than that in the outer region with weaker signals. The source reconstruction is performed after an assumed parametric mass model maps coordinates from the image plane to the source plane with ray-tracing.

3.3.1 The ALMA 300-GHz continuum

When modelling the 300-GHz sub-millimetre data, we adopt iterative steps. To fit the non-parametric source, we first fix the parameters of the lens object according to our parametric mass model (see Sect. 3.2.2), and then use a pixelized Voronoi grid that adapts to

Band	ID	Size (mas × mas)	Peak S/N
814 nm	A	89.4 × 85.6	173
814 nm	B	84.3 × 77.5	151
814 nm	C	91.3 × 86.7	106
814 nm	D	82.4 × 76.6	106
300 GHz	A	540 × 183	116
300 GHz	B	490 × 254	122
300 GHz	C	478 × 216	112
300 GHz	D	426 × 180	75.8
1.5 GHz	A	540 × 257	17.4
1.5 GHz	B&D	443 × 121	28.4
1.5 GHz	C	262 × 161	10.8

Table 2. Apparent sizes of four images of Cloverleaf at different wavelengths, fitted with Gaussian profiles. The sizes are described as (the FWHM of the major axis) × (the FWHM of the minor axis).

Parameters	Definition	Parametric Model	Non-parametric Model
x	R.A. (hh:mm:ss) at mass centre	14:15:46.2384 ^{+ <0.0001} _{- <0.0001}	14:15:46.2325 ^{+ <0.0000} _{- <0.0002}
y	Dec. (° ' ") at mass centre	11:29:43.705 ^{+ <0.001} _{- <0.001}	11:29:43.694 ^{+ <0.001} _{- <0.001}
e_x	Elliptical component x	-0.136 ^{+0.002} _{-0.002}	-0.126 ^{+ <0.001} _{-0.001}
e_y	Elliptical component y	-0.263 ^{+0.002} _{-0.002}	-0.270 ^{+0.003} _{- <0.001}
r	Einstein radius (")	0.645 ^{+0.001} _{-0.001}	0.636 ^{+ <0.001} _{-0.001}
α	Slope	1.897 ^{+0.003} _{-0.003}	1.884 ^{+ <0.001} _{-0.014}
γ_x	Elliptical components x of shear	0.034 ^{+0.001} _{-0.001}	0.043 ^{+ <0.001} _{-0.004}
γ_y	Elliptical components y of shear	-0.054 ^{+0.001} _{-0.001}	-0.057 ^{+ <0.001} _{-0.003}

Table 3. Best fitted parameters of the lens object models derived from the ALMA 300-GHz continuum data.

the mass model’s magnification pattern, giving higher resolutions to areas with higher magnification.

Then, we perform a fit where the source-plane is reconstructed by a brightness-weighted Voronoi (Fig. 3 left) mesh. We fit a new mass model, a power-law ellipsoid (Tessore & Metcalf 2015) with an external shear (shown in Table 3). With the Bayesian inference (Dynesty) integrated within PyAutoLens, we adopt the best fit results and their associated errors as the lens profile (Table 3), which is further used for the non-parametric modelling of the radio data.

3.3.2 The 1.5-, 8-, and 33-GHz continuum

The ALMA 300-GHz continuum image provides strong constraints on our lensing galaxy mass model, therefore we fix the mass model parameters to values derived from this data in order to perform non-parametric fitting at radio bands. Using the same mass model across all wavelengths also ensures source reconstructions can be compared in a uniform way.

For the data from VLA and e-Merlin, the source plane is reconstructed with a magnification-weighted Voronoi mesh, instead of a brightness-weighted one. This is because a magnification based mesh produces an identical grid of Voronoi cells across all three frequency channels, ensuring consistent sampling of the source when calculating the spectral indices pixel by pixel to obtain a spectral indices map. The residual maps at multiple wavelengths are presented in the Appendix B. We measure the radio fluxes within two regions in the source plane, shown as white and red ellipse in Figure 3. The error compromises a 15% absolute flux uncertainty, a ~ 5% error from the uncertainty of the model by running multiple models with all parameters randomly sampled with their probability density distributions,

and a statistical error measured in emission-free regions. The measured quantities of different components on the reconstructed source plane are listed in Table 4.

4 RESULTS

4.1 Spatial distributions of multi-wavelength images

As shown in Sect 3, the HST optical images are point sources dominated by the central AGN. On the other hand, the 300 GHz image (see Fig. 1 right) shows that all four components are much larger than the beam size (see Table 2), indicating that the sub-mm continuum emission has extended structures.

The radio continuum images (shown in Fig. 2) also show resolved extended structures. The B and D components tend to merge when moving to the lower frequency, indicating that the source is lying on the caustics. The other two, components A and C, both also have spatial deviations, not only between different radio bands but also between the images from HST and ALMA.

At 1.5 GHz band, the radio-to-submm spatial offsets are (0.24", -0.01") and (-0.03", 0.24") in R.A. and Dec., for components A and C, respectively. All components in the images of 8 GHz and 33 GHz are irregular with respect to the synthesized beam shapes at the corresponding wavelengths, thus we do not fit their locations with IMFIT.

Among the three radio bands (1.5 GHz, 8 GHz and 33 GHz), the image morphologies are not identical. The 1.5 GHz image shows almost no emission from the host galaxy, while both 8 and 33 GHz radio images show detections at the same position. This suggests a

Component	Frequency (GHz)	Flux (μJy)	Size ($'' \times ''$)	Peak Position (R.A., Dec.)
host galaxy	300	$2.0 \pm 0.3 [\pm 0.3] \times 10^3$	0.12×0.11	(14:15:46.2378, 11:29:43.659)
host galaxy	33	$4.8 \pm 1.3 [\pm 0.7]$	0.14×0.11	(14:15:46.2364, 11:29:43.659)
host galaxy	8	$3.1 \pm 1.0 [\pm 0.5]$	0.20×0.11	(14:15:46.2383, 11:29:43.698)
host galaxy	1.5	$26 \pm 10 [\pm 4]$	-	(14:15:46.2388, 11:29:43.689)
radio lobe	33	$4.7 \pm 1.0 [\pm 0.7]$	0.15×0.086	(14:15:46.2315, 11:29:43.787)
radio lobe	8	$6.1 \pm 1.2 [\pm 0.9]$	0.12×0.046	(14:15:46.2315, 11:29:43.781)
radio lobe	1.5	$1.1 \pm 0.2 [\pm 0.2] \times 10^2$	0.12×0.045	(14:15:46.2299, 11:29:43.781)

Table 4. Measured quantities of the Cloverleaf components in the source plane at different wavelengths, where the fluxes are obtained within the ellipses in Fig. 3, and the intrinsic sizes are described in (the FWHM of the major axis) \times (the FWHM of the minor axis). The error consists of contributions from statistical error and model uncertainty, and from the absolute calibration error (15%, shown in the squared bracket).

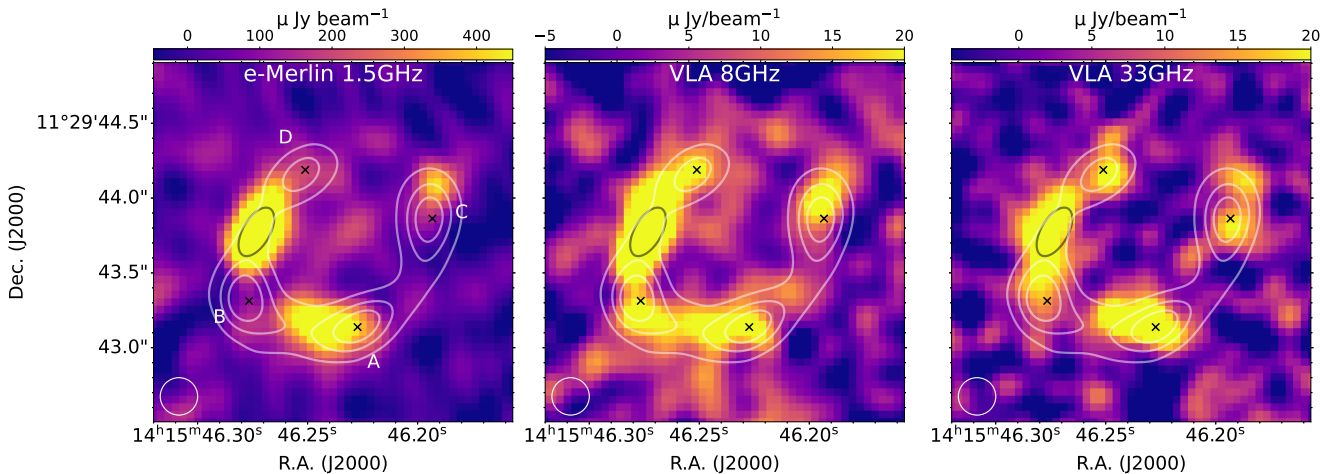


Figure 2. Radio emission of Cloverleaf at 1.5 GHz (left), 8 GHz (middle), and 33 GHz (right) respectively. The white lines are the contours of the ALMA dust continuum. The black crosses show the peak positions of four components in the HST data, starting 25σ , with steps of 30σ . The black ellipse is the area we select to obtain the fluxes at each band for the SED of the radio lobe in the lens plane.

differential lensing effect and multiple energy sources among different wavelengths.

4.2 The discovery of a radio lobe

As shown in the reconstructed image of the source plane at 300 GHz of Cloverleaf (Fig. 3), the cold dust emission shows an extended disk-like structure of $0.115'' \times 0.109''$ in FWHM ($0.946 \text{ kpc} \times 0.897 \text{ kpc}$) rather than a point source.

The peak of this dust continuum has an $S/N \sim 27$, with substructures around it. The majority of the host galaxy emission is distributed in the central region, inside the inner caustics, while a small clump is located in the southwest to the centre. Due to the uncertainty of the lens model, several emission clumps outside the caustics have less fidelity.

All reconstructed radio images show extended emission to the northwest of the dust continuum core, at a projected distance of $\sim 1.15 \text{ kpc}$ ($0.14''$) away from the centre of the host galaxy. The peaks of this radio component are roughly consistent among different radio wavebands. This indicates a single-sided radio lobe launched from the host galaxy, with a comparable size of the host galaxy at 300 GHz. The FWHMs of this radio clump, fitted with Gaussian profiles, are $0.98 \text{ kpc} \times 0.37 \text{ kpc}$, $0.95 \text{ kpc} \times 0.38 \text{ kpc}$, and $1.23 \text{ kpc} \times 0.68 \text{ kpc}$, at 1.5 GHz, 8 GHz, and 33 GHz, respectively.

On the other hand, on the source plane, the 1.5 GHz radio emission

from the host galaxy is almost negligible, while the 8 GHz and 33 GHz images show radio emission at the location of the host galaxy, with their S/N s of 3.1 and 3.7, respectively.

To verify the consistency between the optical data and our parametric/non-parametric models, we invert a simple point source to the image plane, with lens mass models derived from parametric and non-parametric fitting. Both positions and fluxes of the point source are adopted from the result first fitted with the HST data. For both parametric and non-parametric models, the positions of the simulated point source (Fig. 1) match well with all four images in the HST data, within 0.5-pixel size. This indicates that our models are reliable.

4.3 Spectral indices of the radio continuum

The multiple-band radio maps allow us to probe the spectral energy distributions (SEDs) of both the host galaxy and the radio lobe. To evaluate the impact of the differential magnification effect and to probe the power sources of the radio emission, we construct SEDs derived from both the image plane and the source plane (see Fig. 4).

We first measure radio fluxes from regions shown in the lens plane (Fig. 2) and the source plane (Fig. 3) for 1.5, 8, and 33 GHz, respectively. The regions adopted to measure fluxes on the source plane are shown in Fig. 3.

On the image plane, however, the emission from the host galaxy

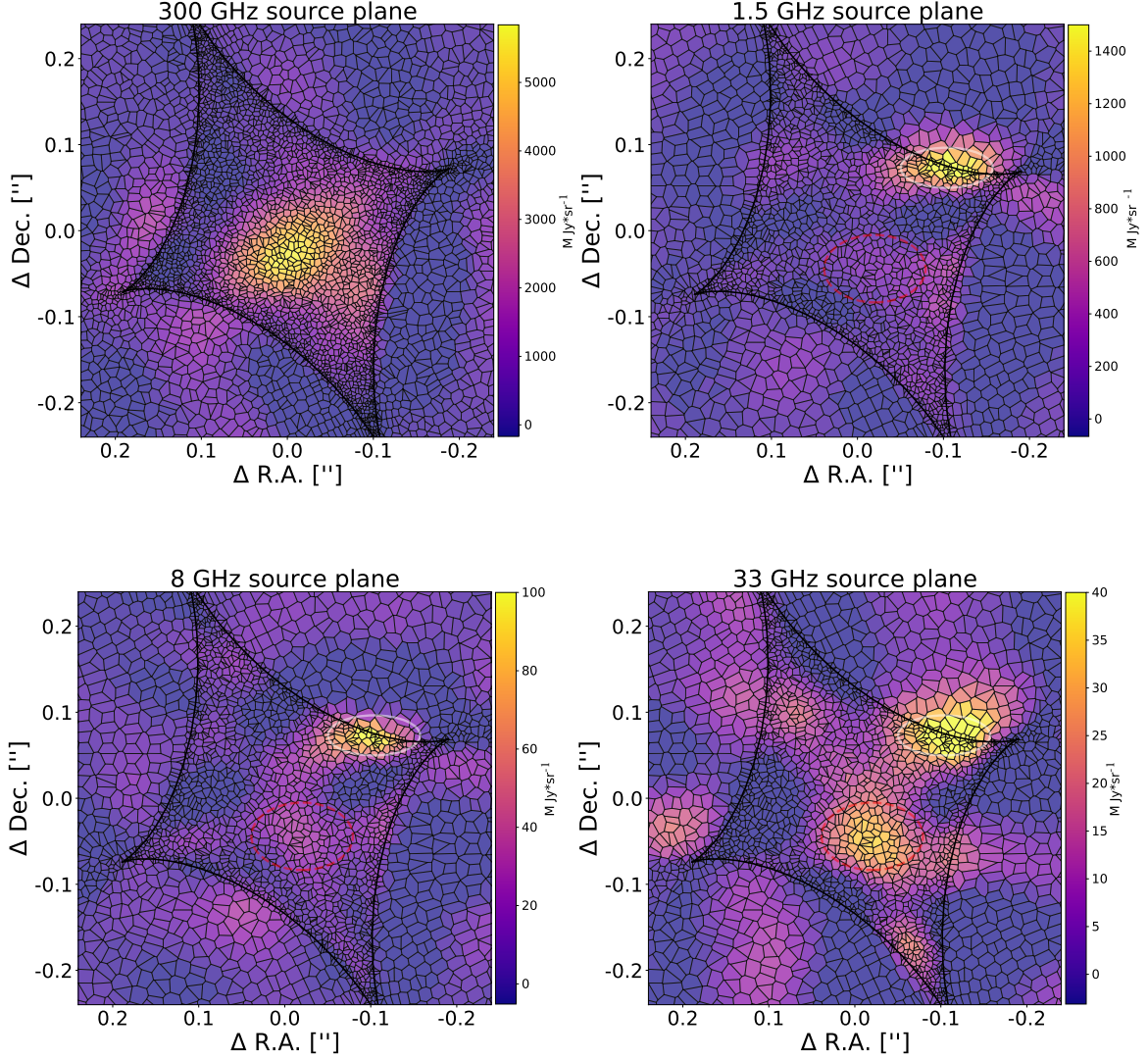


Figure 3. Reconstructed source planes of Cloverleaf at multiple bands: top left: sub-millimetre continuum at 300 GHz; top right: radio continuum at 1.5 GHz; bottom left: radio continuum at 8 GHz; bottom right: radio continuum at 33 GHz. The black solid line is the inner caustics. The centre is on (14:15:46.2384^h, 11:29:43.705) in the J2000.0 equatorial system of coordinates. The white solid ellipse and the red dashed ellipse are the areas to draw fluxes for SEDs of the radio lobe and the host galaxy respectively.

and the radio lobe do not show distinct spatial offsets between each other. The radio emission of components B and D tend to merge together, indicating that this emission component is lying on the caustics (Appendix A), where the radio lobe populates while the host galaxy does not. Therefore, to eliminate contamination from the host galaxy, we choose this region (shown as black ellipses in Fig. 2) on the image plane and construct the SED of the lensed radio lobe. On the other hand, we adopt beam-sized regions at the peaks of the four image components to measure fluxes from the host galaxy. We then sum up fluxes from all four components to increase the S/N.

Then we fit spectral indices with fluxes from all three radio bands, which are shown in orange lines of Fig. 4. It seems that none of the SEDs can be fitted with a single power-law at all positions, especially for the host galaxy. This may indicate a non-negligible contribution from free-free emission or dust emission at 33 GHz

(rest-frame 115 GHz). Therefore, we also fit the spectral indices with only the 1.5 and 8 GHz data and show them with blue lines of Fig. 4.

We also use the e-Merlin data only, which covers 1.25 – 1.77 GHz bandwidth, to fit a spectral index map (Fig. 5). We measured the fluxes of the e-Merlin data within a region of S/N > 16 and derive the spectral index of the merging components B and D, which is adopted as the spectral index of the lensed radio lobe at 1.5 GHz in the image plane. All derived spectral indices, for both the host galaxy and the radio lobe, are listed in Table 5.

Although the average slope of the e-Merlin spectral index map is consistent with that obtained with $\alpha_{1.5}^8$ in the whole region, it also shows a systematic gradient of the radio slope from the east to the west direction. This indicates that the radio lobe may have complex structures or physical processes that need higher-resolution data to study in detail.

From the flux maps shown in Fig. 3, we fit a spectral index map

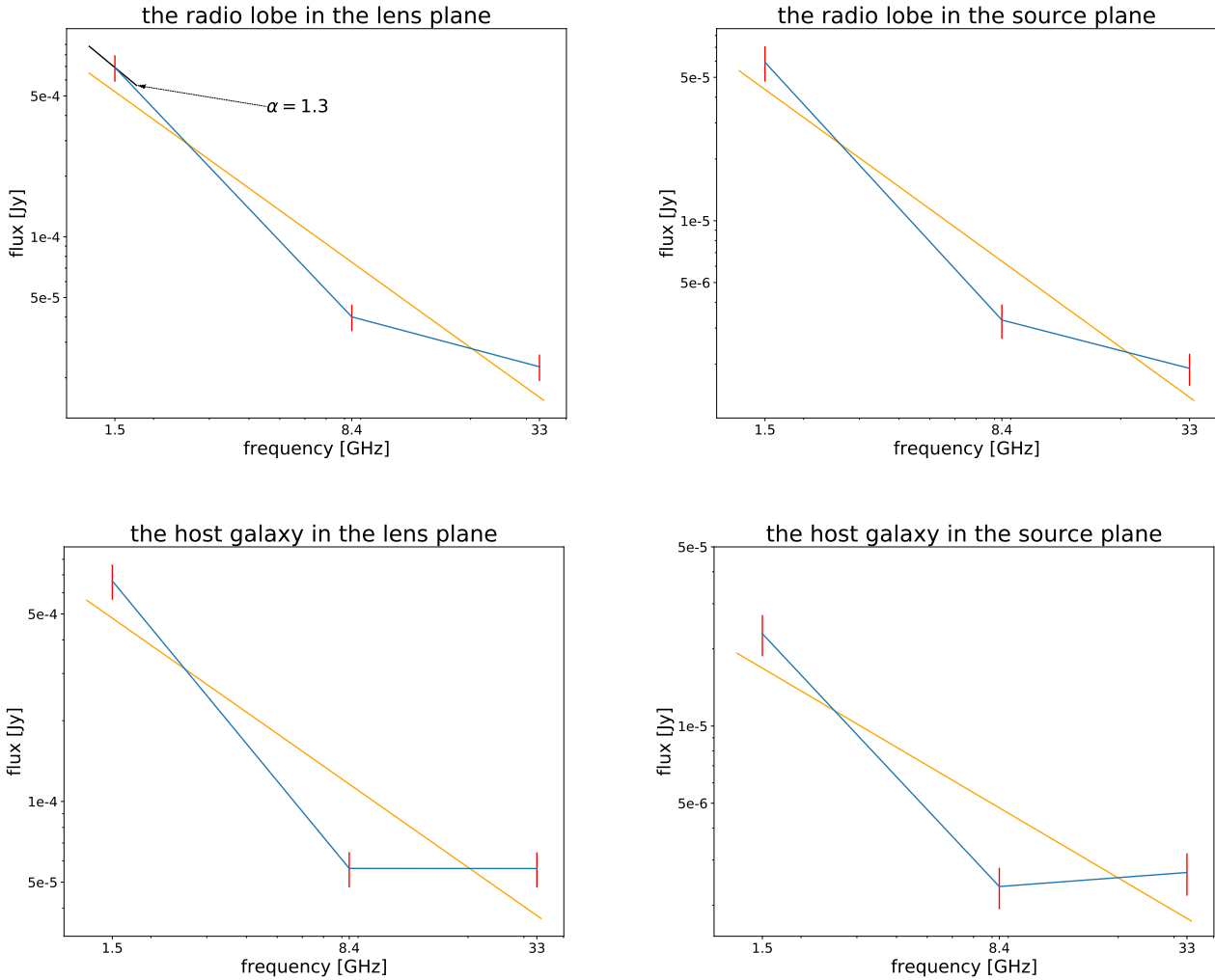


Figure 4. Spectral energy distributions (SEDs) of the radio lobe and the host galaxy of Cloverleaf. *Top-Left:* SED of the radio lobe in the lens plane. *Top-Right:* SED of the radio lobe in the source plane. *Bottom-Left:* SED of the host galaxy in the lens plane. *Bottom-Right:* SED of the host galaxy in the source plane. Radio fluxes are measured from the regions shown in the lens plane (Fig. 2) and the source plane (Fig. 3). Blue lines are the line charts. Orange lines show the best linear fitting result for all three frequencies. The black line in the top-left panel shows the spectral index of the radio lobe in the lens plane derived from the 1.5 GHz e-Merlin data. All derived spectral indices are listed in Table 5.

(Fig. 6, by the opposite sign convention of α) using de-lensed flux maps on the source plane. As shown in Fig. 6, we fit a power-law for all pixels with an S/N > 3.5 at 8 GHz, 1.5 GHz and 33 GHz maps. The spectral index map shows flatter SED at the host galaxy position, while steeper SED at the radio lobe.

5 DISCUSSION

5.1 Differential Lensing Effects

Compared with the lensed image of Cloverleaf at ~ 300 GHz, those at radio bands have different spatial distributions, also known as differential lensing (e.g., Serjeant 2012; Er 2014), which indicates that the emission distributions at different bands are different from one another in the source plane. This can be inferred directly from the reconstructed source planes (see Fig. 3). All reconstructed radio images contain radio structures on scales of $\sim 0.9 \times 0.4$ kpc, on the northwest part of the inner caustics.

5.2 Possibility to be a jet in the foreground?

One may also ask if the radio feature comes from the foreground lens galaxy, instead of the background source galaxy. First, the multiple components shown in all radio bands indicate that it is unlikely to be multiple jets from the centre. Second, the spatial distributions of all radio components are highly consistent with the scenario that the radio structure locates on the caustics, i.e. merging between lensed components (Appendix A). Therefore, we suggest that this radio structure should reside in the source plane and originate from the position on the northwest part of caustics.

5.3 Why One-sided?

On the other hand, the radio source only presents on one side of the host galaxy, while the other side shows almost no signal. Depending on the geometry, the other side of the radio lobe might be too faint to be detected due to Doppler dimming (Lanzetta et al. 2002) caused by

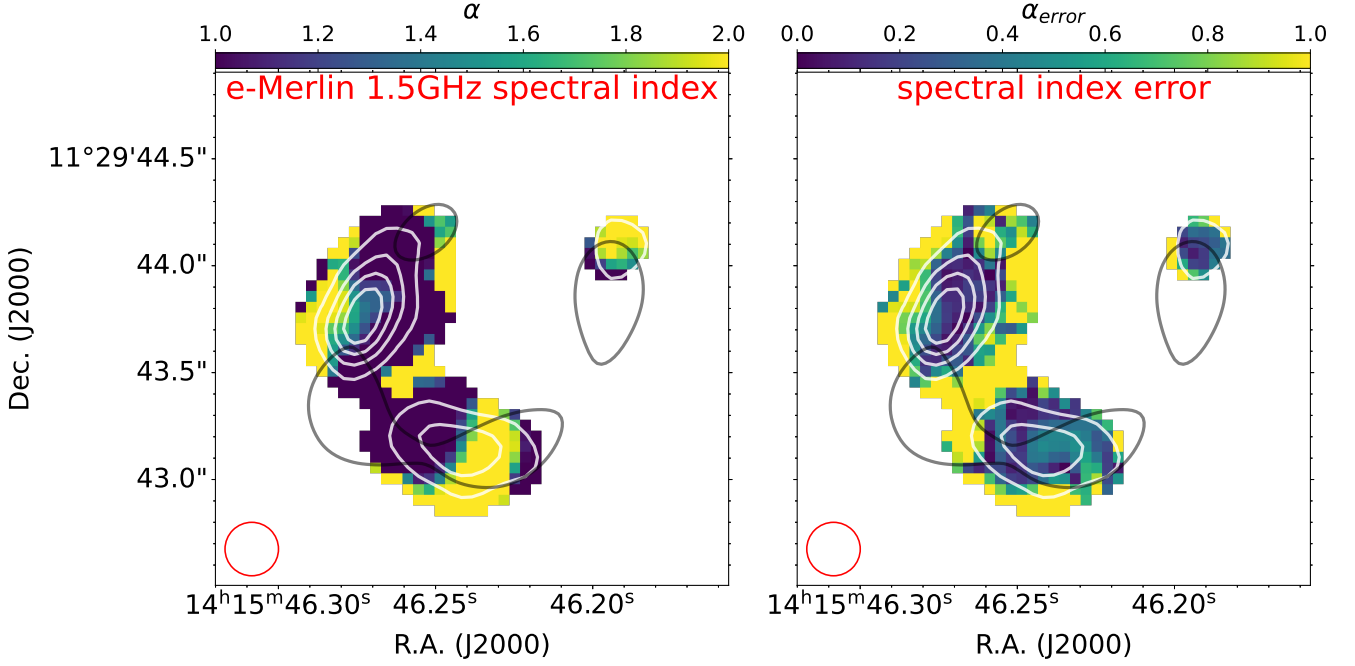


Figure 5. Spectral index map (Left) and its error map (Right) in the lens plane at 1.5 GHz. The white and black lines are the contours of the image at 1.5 GHz and 300 GHz, respectively. The red circles represent the beam sizes.

Component	Plane	$\alpha_8^{1.5}$	α_{33}^8	α_{total}
radio lobe	lens	1.66 ± 0.12	0.42 ± 0.16	1.13 ± 0.35
radio lobe	source	1.68 ± 0.16	0.40 ± 0.19	1.12 ± 0.36
host galaxy	lens	1.43 ± 0.12	0.00 ± 0.16	0.83 ± 0.41
host galaxy	source	1.32 ± 0.15	-0.09 ± 0.19	0.73 ± 0.40

Table 5. Spectral indices of different components in the lens plane and the source plane: α_{total} is the spectral index of the best linear fit, considering fluxes in all three radio bands.

a large project angle, or simply does not exist. In any case, if the other side of the radio lobe exists, it should lead to emission populating the area between components A and C (see Appendix A). Future deeper observations would be the key to verifying this scenario.

5.4 The skewness of the SEDs

As shown in Fig. 4 and Table 5, the SEDs of the radio lobe in both lens plane and source plane have similar spectral indices, which become flatter at higher frequencies. However, the SED of a radio lobe should be steeper at higher frequencies, at which the energy loss rate is higher than that at lower frequencies.

In contrast, the SED of the host galaxy shows higher fluxes at 33 GHz (rest frequency, $f_{rest} \sim 110$ GHz) than that at 8 GHz ($f_{rest} \sim 28.5$ GHz). Considering the flat spectral indices (see Fig. 6) and the skewed SED at the position of the host galaxy, we suggest that the emission from this area at 33 GHz could be dominated by the free-free or/and dust emission.

However, on the radio lobe position, the 33 GHz emission also shows a quite strong emission, indicating that its 33 GHz emission may also have contributions from thermal origins. The dust continuum does not show evidence of image merging, thus the radio lobe emission at 33 GHz may not originate from dust. If we adopt an extreme dust emissivity slope index of $\beta = 1$, the contribution of dust

at 33 GHz would be $\sim 1 \mu\text{Jy}$ within the black ellipse in Fig. 2, extrapolated from the 300 GHz dust emission. This is far from enough to support the detected 33 GHz emission. We suggest that free-free emission of gas, which is ionized by the jet (Ghavamian & Hartigan 1998), may contribute to the abnormally high flux of the radio lobe at 33 GHz.

5.5 Spectral Ageing of the Radio Lobe

Assuming that the 8 GHz and 1.5 GHz radio emission at the radio lobe is dominated by the synchrotron emission, we estimate the age of this radio lobe. Given that the spectral index between 8 GHz and 1.5 GHz is very steep ($\alpha_8^{1.5} = 1.7$), while the spectral index at 1.5 GHz (derived from the e-Merlin data only) is however flatter ($\alpha = 1.3$), the turnover point (at a frequency ν_0) of this synchrotron spectrum would be expected to be between 1.5 GHz and 8 GHz. In other words, the electrons emitting at ν_0 in the observer frame have cooled down.

Rybicki & Lightman (1979) suggested that a relativistic electron has a peak synchrotron emission at $0.3\nu_c$ (ν_c is the critical frequency):

$$\nu_c = \frac{3\gamma^2 eB}{4\pi m_e c}, \quad (1)$$

where γ , e , and m_e are the Lorentz factor, the electric charge, and

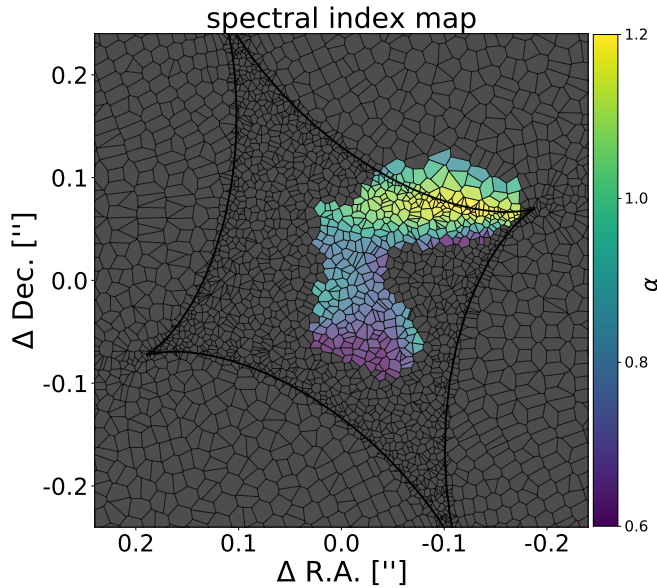


Figure 6. Spectral index map in the source plane: The black solid line is the inner caustics. The centre is on (14:15:46.2384^h, 11:29:43.705) in the equatorial system of coordinates.

the mass of an electron, B is the magnetic field strength, and c is the speed of light in the vacuum. The lifetime of this electron can be obtained with

$$t = \frac{3m_e^3 c^5}{2e^4 B^2 \gamma}. \quad (2)$$

Assuming a magnetic field strength of $3 \mu\text{G}$ found for the average conditions of the Milky Way with Wilkinson Microwave Anisotropy Probe (Jansson & Farrar 2012) and

$$0.3\nu_c = (1+z)\nu_0, \quad (3)$$

where ν_0 is the turnover point of the local observing frequency. The lifetime of electrons emitting at 8 GHz in the observer frame is estimated to be about ~ 20 Myr. Besides, for electrons emitting at 1.5 GHz in the observer frame, that would be about 50 Myr. Given that the turnover point frequency is between 1.5 GHz and 8 GHz, the estimated age of this radio lobe is in the range of 20–50 Myr.

5.6 Feedback Mode of Cloverleaf

This radio lobe is located at a projected distance of ~ 1.15 kpc ($0.14''$) from the galaxy centre, with a size similar to that of the host galaxy at 33 GHz. From the morphology of this radio lobe, it seems more likely to be a Fanaroff-Riley class II (FR II) jet. These are consistent with radio lobe features found in massive radio galaxies (Fabian 2012), however, Cloverleaf seems to have a lower galaxy mass than those massive galaxies (Solomon et al. 2003).

On the other hand, given the very small lifetime of the radio lobe (20–50 Myr old), the kinetic energy residing in the jet could severely heat up the gas and drive strong negative feedback to the star formation in Cloverleaf. However, based on the optical data, the

AGN of Cloverleaf prevents evidence that it is in the quasar mode at its current stage (Magain et al. 1988). Given its strong ongoing starburst, likely driven by the interaction with a neighbouring gas-rich galaxy (Stacey & Arrigoni Battaia 2022), it is possible that the Cloverleaf QSO is in a transition phase between the radio mode and the quasar mode.

It is possible that the AGN of Cloverleaf was on radio mode about 20–50 Myr ago, and then it was disturbed by the gravitational potential of the interaction from the neighbourhood, which caused the starburst and then switched off the quasar feedback mode. It is also possible that the starburst has kept a high accretion rate for the central AGN, and has kept the quasar mode for a long time. Until now, after a substantial starburst that effectively consumed molecular gas, it turns on the radio jet and starts the radio mode feedback.

The previous survey for gravitational lensed radio lobes was found inefficient (Lehár et al. 2001; Haarsma et al. 2005), so our discovery of a radio lobe of the Cloverleaf system offers a unique case. High angular resolution observations of both radio continuum and molecular gas tracers in the future, which help resolve the jet structure and gas kinematics, could throw light on the co-existence of both modes of AGN feedback.

6 CONCLUSION

With high angular resolution photometric data at optical, sub-mm, and radio wavelengths, we reconstructed multi-band source images of the gravitational lensed Cloverleaf QSO, with both parametric and non-parametric modelling. From the differential lensing effect, we discovered a single-sided radio lobe, with a size of ~ 1.5 –2 kpc, located at ~ 1.2 kpc to the northwest of Cloverleaf. From the spectral indices at radio bands, we estimate an age of 20–50 Myr, indicating that the feedback from Cloverleaf QSO is likely converting from the quasar mode to the radio mode. This provides a unique case for the galaxy-SMBH co-evolution studies at high redshifts.

The joint analysis of the high spatial resolution images at multiple wavelengths provides a powerful tool to reconstruct the morphological components of the radio galaxies at high redshift. The high-quality data from future Chinese Space Station Telescope and Square Kilometer Array surveys would also be benefited from non-parametric lens modeling for a large sample of such lensed radio galaxies.

ACKNOWLEDGEMENTS

Based on observations made with the NASA/ESA Hubble Space Telescope, and obtained from the Hubble Legacy Archive, which is a collaboration between the Space Telescope Science Institute (STScI/NASA), the Space Telescope European Coordinating Facility (ST-ECF/ESAC/ESA) and the Canadian Astronomy Data Centre (CADNRC/CSA). LZ appreciates Yunwei Deng and Chengjiang Yin for their technical helps. ZYZ and LZ acknowledge support of the National Natural Science Foundation of China (NSFC) under grants No. 12041305, 12173016. ZYZ and LZ acknowledge the Program for Innovative Talents, Entrepreneur in Jiangsu. ZYZ and LZ acknowledge the science research grants from the China Manned Space Project with NO.CMS-CSST-2021-A08. DDX acknowledges the NSFC Grant 12073013. This work is supported by the China Manned Space Project (No. CMS-CSST-2021-A07). RL acknowledges the support of National Nature Science Foundation of China (Nos 11988101, 11773032, 12022306), the support from the Ministry of Science and Technology of China (Nos. 2020SKA0110100),

the science research grants from the China Manned Space Project (Nos. CMS-CSST-2021-B01, CMS-CSST-2021-A01), CAS Project for Young Scientists in Basic Research (No. YSBR-062). Z.-C. Z. is supported by the National Natural Science Foundation of China (Grant Nos. 12233002, 11873030, 12041306).

This work used the following software: Autolens (Nightingale & Dye 2015; Nightingale et al. 2018, 2021b), CASA (McMullin et al. 2007), SAOimageDS9 (Joye & Mandel 2003), astropy (Astropy Collaboration et al. 2013; Price-Whelan et al. 2018), dynesty (Speagle 2020), corner (Foreman-Mackey 2016), emcee (Foreman-Mackey et al. 2013), matplotlib (Hunter 2007), numpy (van der Walt et al. 2011), pyautofit (Nightingale et al. 2021a), pyllops (Ravasi & Vasconcelos 2019), python (Van Rossum & Drake 2009), scipy (Virtanen et al. 2020)

DATA AVAILABILITY

All data adopted in this work are publicly available in corresponding data archival systems of HST, ALMA, VLA, and e-Merlin.

REFERENCES

- Alexander D. M., Swinbank A. M., Smail I., McDerimid R., Nesvadba N. P. H., 2010, *MNRAS*, **402**, 2211
- Angonin M. C., Remy M., Surdej J., Vandierriest C., 1990, *A&A*, **233**, L5
- Astropy Collaboration et al., 2013, *A&A*, **558**, A33
- Barvainis R., Maloney P., Antonucci R., Alloin D., 1997, *ApJ*, **484**, 695
- Bertin E., Mellier Y., Radovich M., Missonnier G., Didelon P., Morin B., 2002, in Bohlender D. A., Durand D., Handley T. H., eds, *Astronomical Society of the Pacific Conference Series Vol. 281, Astronomical Data Analysis Software and Systems XI*. p. 228
- Cano-Díaz M., Maiolino R., Marconi A., Netzer H., Shemmer O., Cresci G., 2012, *A&A*, **537**, L8
- Cattaneo A., Best P. N., 2009, *MNRAS*, **395**, 518
- Cattaneo A., et al., 2009, *Nature*, **460**, 213
- Chantry V., Magain P., 2007, *A&A*, **470**, 467
- Churazov E., Sazonov S., Sunyaev R., Forman W., Jones C., Böhringer H., 2005, *MNRAS*, **363**, L91
- Cutri R. M., et al., 2003, *VizieR Online Data Catalog*, p. II/246
- Ding X., Silverman J. D., Onoue M., 2022, arXiv e-prints, p. arXiv:2209.03359
- Dunn J. P., et al., 2010, *ApJ*, **709**, 611
- Er X., 2014, *MNRAS*, **444**, 2685
- Fabian A. C., 2012, *ARA&A*, **50**, 455
- Farrar D., et al., 2012, *ApJ*, **745**, 178
- Ferrarese L., Ford H., 2005, *Space Sci. Rev.*, **116**, 523
- Foreman-Mackey D., 2016, *The J. Open Source Softw.*, **1**, 24
- Foreman-Mackey D., Hogg D. W., Lang D., Goodman J., 2013, *Publ. Astron. Soc. Pac.*, **125**, 306
- Ghavamian P., Hartigan P., 1998, *ApJ*, **501**, 687
- Gopal-Krishna Wiita P. J., 2001, *ApJ*, **560**, L115
- Granato G. L., Danese L., Franceschini A., 1996, *ApJ*, **460**, L11
- Haarsma D. B., et al., 2005, *AJ*, **130**, 1977
- Hunter J. D., 2007, *Comput Sci Eng*, **9**, 90
- Jansson R., Farrar G. R., 2012, *ApJ*, **761**, L11
- Joye W. A., Mandel E., 2003, in Payne H. E., Jedrzejewski R. I., Hook R. N., eds, *Astronomical Society of the Pacific Conference Series Vol. 295, Astronomical Data Analysis Software and Systems XII*. p. 489
- Kayser R., Surdej J., Condon J. J., Kellermann K. I., Magain P., Remy M., Smette A., 1990, *ApJ*, **364**, 15
- Kneib J. P., Alloin D., Mellier Y., Guilloateau S., Barvainis R., Antonucci R., 1998, *A&A*, **329**, 827
- Kormendy J., Ho L. C., 2013, *ARA&A*, **51**, 511
- Lanzetta K. M., Yahata N., Pascarella S., Chen H.-W., Fernández-Soto A., 2002, *ApJ*, **570**, 492
- Lawrence C. R., 1996, in Kochanek C. S., Hewitt J. N., eds, *Astrophysical Applications of Gravitational Lensing*. p. 299
- Lehár J., Buchalter A., McMahon R. G., Kochanek C. S., Muxlow T. W. B., 2001, *ApJ*, **547**, 60
- Li J., et al., 2021, *ApJ*, **918**, 22
- Lucas R. A., Rose S., 2021, in , Vol. 10, *ACS Data Handbook v. 10.0*. p. 10
- Magain P., Surdej J., Swings J. P., Borgeest U., Kayser R., 1988, *Nature*, **334**, 325
- McMullin J. P., Waters B., Schiebel D., Young W., Golap K., 2007, in Shaw R. A., Hill F., Bell D. J., eds, *Astronomical Society of the Pacific Conference Series Vol. 376, Astronomical Data Analysis Software and Systems XVI*. p. 127
- McNamara B. R., Nulsen P. E. J., 2007, *ARA&A*, **45**, 117
- Moe M., Arav N., Bautista M. A., Korista K. T., 2009, *ApJ*, **706**, 525
- Nesvadba N. P. H., Lehnert M. D., De Breuck C., Gilbert A. M., van Breugel W., 2008, *A&A*, **491**, 407
- Nesvadba N. P. H., Polletta M., Lehnert M. D., Bergeron J., De Breuck C., Lagache G., Omont A., 2011, *MNRAS*, **415**, 2359
- Nightingale J. W., Dye S., 2015, *MNRAS*, **452**, 2940
- Nightingale J. W., Dye S., Massey R. J., 2018, *MNRAS*, **478**, 4738
- Nightingale J. W., Hayes R. G., Griffiths M., 2021a, *J. Open Source Softw.*, **6**, 2550
- Nightingale J. W., et al., 2021b, *J. Open Source Softw.*, **6**, 2825
- Planck Collaboration et al., 2020, *A&A*, **641**, A6
- Price-Whelan A. M., et al., 2018, *AJ*, **156**, 123
- Prochaska J. X., Hennawi J. F., 2009, *ApJ*, **690**, 1558
- Ravasi M., Vasconcelos I., 2019
- Rybicki G. B., Lightman A. P., 1979, *Radiative processes in astrophysics*
- Saez C., Chartas G., Brandt W. N., 2009, *ApJ*, **697**, 194
- Schmidt M., Green R. F., 1983, *ApJ*, **269**, 352
- Serjeant S., 2012, *MNRAS*, **424**, 2429
- Shi F., Li Z., Yuan F., Zhu B., 2021, *Nature Astronomy*, **5**, 928
- Silverman J. D., et al., 2019, *ApJ*, **887**, L5
- Solomon P., Vanden Bout P., Carilli C., Guelin M., 2003, *Nature*, **426**, 636
- Speagle J. S., 2020, *MNRAS*, **493**, 3132
- Springel V., Di Matteo T., Hernquist L., 2005, *MNRAS*, **361**, 776
- Stacey H. R., Arrigoni Battaia F., 2022, *MNRAS*, **517**, L11
- Tessore N., Metcalf R. B., 2015, *A&A*, **580**, A79
- Turnshek D. A., Foltz C. B., Grillmair C. J., Weymann R. J., 1988, *ApJ*, **325**, 651
- Turnshek D. A., Lupie O. L., Rao S. M., Espey B. R., Sirola C. J., 1997, *ApJ*, **485**, 100
- Van Rossum G., Drake F. L., 2009, *Python 3 Reference Manual*. CreateSpace, Scotts Valley, CA
- Venturini S., Solomon P. M., 2003, *ApJ*, **590**, 740
- Virtanen P., et al., 2020, *Nature Methods*, **17**, 261
- Weiß A., Henkel C., Downes D., Walter F., 2003, *A&A*, **409**, L41
- Wolf C., Wisotzki L., Borch A., Dye S., Kleinheinrich M., Meisenheimer K., 2003, *A&A*, **408**, 499
- van der Walt S., Colbert S. C., Varoquaux G., 2011, *Comput Sci Eng*, **13**, 22

APPENDIX A: MOCK DATA

In Figure A1, we present the mock data of the lensing system of Cloverleaf, to simulate the response of a background source with a Sérsic profile. The lens model is the same as the one in our non-parametric model. The source is a Sérsic ellipsoid moving from the north-west part to the south-east part of the inner caustics in the source plane, and its centre is marked with red crosses as moving.

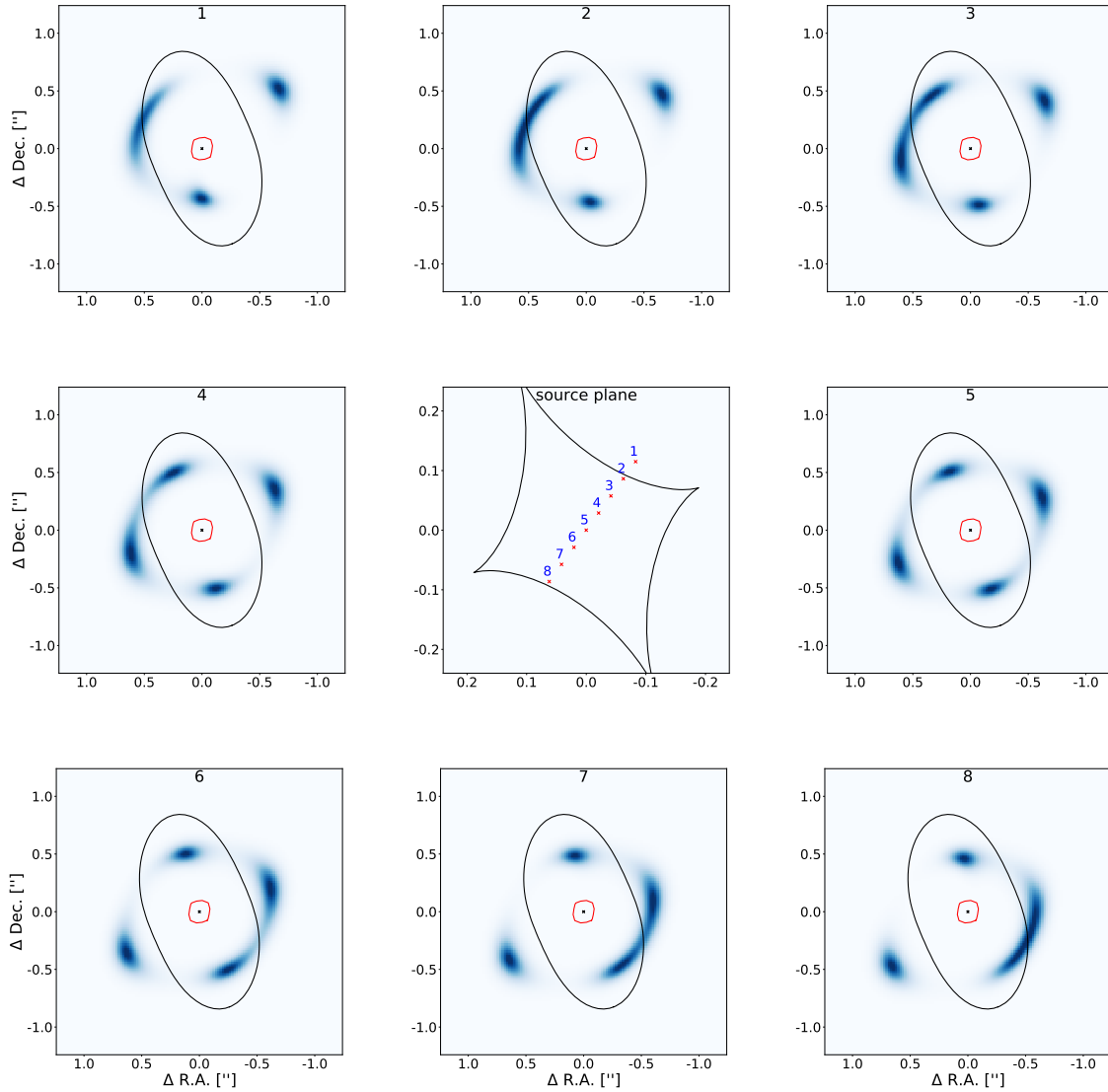


Figure A1. Mock data of this lensing system: The lens model is the same as the one in our non-parametric model. The source is a Sérsic ellipsoid moving from the north-west part to the south-east part of the inner caustics in the source plane, and its centre is marked with red crosses as moving. The black solid line and the red solid line are the outer and the inner critical curve (which is incorrect due to the numerical issue and should be a point) in the lens plane respectively. The black solid line (diamond-shape) in the source plane is the inner caustics.

APPENDIX B: RESIDUAL

In Figure B1, we present the residual maps of our lensing models of the 300 GHz, 1.5 GHz, 8 GHz, and 33 GHz data.

This paper has been typeset from a $\text{\TeX}/\text{\LaTeX}$ file prepared by the author.

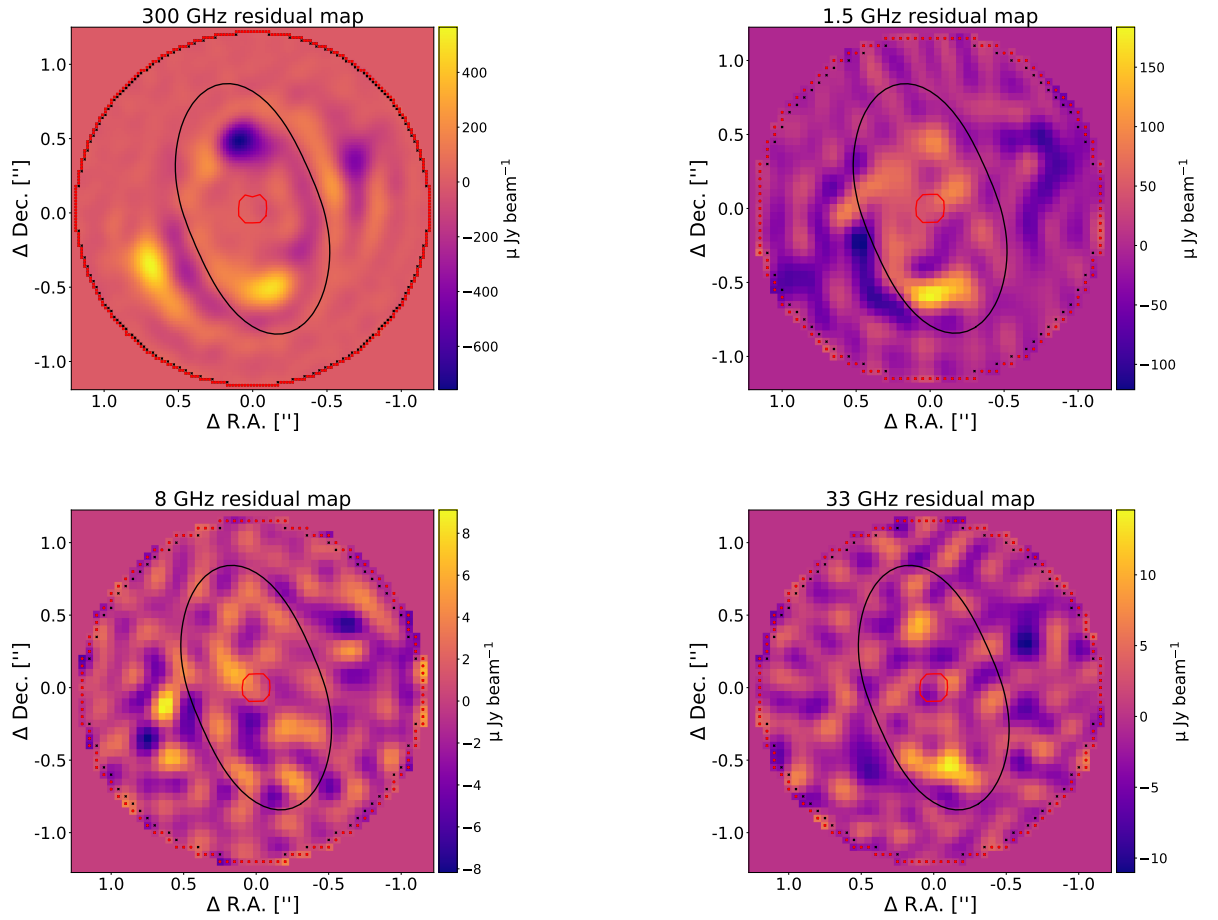


Figure B1. Residual maps of non-parametric models at 300 GHz, 1.5 GHz, 8 GHz, and 33 GHz: The red dot circle is the mask. The black solid line and the red solid line are the outer critical curve and the inner critical curve (which is incorrect due to the numerical issue and should be a point) respectively.